TECHNISCHE UNIVERSITÄT WIEN

BACHELORARBEIT

Optimization of an Advanced Catcher-QCM Setup for Sputtering Yield Measurements of He^+ and Ar^+ Ions on Enstatite

ausgeführt am Institut für Angewandte Physik
der Technischen Universität Wien

unter der Anleitung von
Dipl.-Ing. Johannes Brötzner, BSc und
Univ.-Prof. Dr.techn. Friedrich Aumayr

durch
Benjamin Cserveny
11924466

Landstraßer Hauptstraße 67
1030 Wien

Abstract

Unlike Earth, most celestial bodies like moons, planets and asteroids do not feature a protecting atmosphere. As a consequence, their surfaces are subject to continuous particle bombardment primarily by solar wind ions among others. Under these harsh conditions, surface atoms are constantly ejected into space forming a tenuous layer of a collisionless gas, which is referred to as an exosphere. A detailed analysis of this cosmic dust may provide deeper insight into the composition and properties of the body's surface. Multiple models that predict the formation of these exospheres already exist. However, more precise input about the individual ejection processes are needed to be able to interpret numerical results in comparison with data gathered during space missions. This thesis aims to experimentally acquire data as input for the sputtering contribution to exosphere formation models.

Therefore, the angular distribution of sputtered enstatite ($MgSiO_3$) was investigated using the quartz crystal microbalance (QCM) technique. The target consists of a gold coated quartz on which a thin layer of enstatite was deposited via pulsed laser deposition (PLD). A pellet made from ground and compressed enstatite was also irradiated due to its more realistic properties when it comes to surface roughness and crystallinity. This demands the introduction of a catcher QCM with the ability to perform circular movements around the target holder to collect the sputtered particles.

Past sputtering yield measurements of this kind indicated that the sticking coefficients of the ejecta to the catcher surface are not constant throughout a measurement cycle, but depend on the fluence that is applied. Several adaptations to the experimental setup were made in an effort to eliminate the fluence dependency of these sticking probabilities. Experiments were carried out using a 2 keV Ar^+ ion beam to confirm the success of these changes. Additional irradiations using a 4 keV He^+ ion beam were performed to obtain more relevant sputtering data. It is assumed that the improvements made on the setup as well as the experience gained during this project will constitute the basis for future He^+ irradiations at the Institute of Applied Physics of the TU Wien.

Contents

1 Introduction

1.1 Motivation

Most celestial bodies do not possess a protective atmosphere and are therefore subject to external influences leading to alterations in their surface structure and composition, generally referred to as space weathering [1]. These changes can be attributed to (micro-) meteoroid impacts, interaction with electromagnetic radiation, thermal desorption and bombardment with solar wind ions. One can trace back the Moon's dark rims on regolith grains in Lunar soil [2, 3] and the reddened absorption bands in mercury's reflectance spectrum [1] primarily to solar wind ion irradiation and micro meteoroid impacts on their surfaces. Not only does space weathering cause changes in surface appearance, but it also leads to the ejection of surface atoms. Those particles with less energy than required for escaping the body's gravitational field will eventually follow a ballistic trajectory and form a tenuous layer of collisionless gas. If a steady state between incoming and sputtered particles is reached, the escaping particles will also contribute to the formation of this layer, which is referred to as the *exosphere* [4]. Since the composition of the exosphere heavily depends on the surface properties, a detailed analysis of this tenuous gas may yield valuable information regarding the surface characteristics of the celestial object. One way to acquire such data is to perform flyby missions like the MESSENGER mission to Mercury by NASA in 2004-15 [5]. The BepiColombo spacecraft was launched in 2018 by ESA and JAXA to further investigate Mercury's surface composition among other properties of interest [6]. Flyby missions in general represent a very feasible kind of sampling since they do not require landing on the object of interest at the risk of crashing the spacecraft.

The main source of ion precipitation on the Moon is the solar wind. It is a continuous stream of plasma that escapes the sun's corona due to the high temperatures and the sun's magnetic field. Protons (H^+) and alpha particles ($^4He^{2+}$) account for up to 99% of the solar wind flux with energies of approximately 1 keV/amu.[7]. Especially in the polar regions of Mercury, solar wind ions combine with ions of its own magnetosphere and contribute to exosphere formation [8].

All experiments described in this thesis were conducted on enstatite ($MgSiO_3$), which serves as an analogue material for hermean surface regolith. It is part of the pyroxene group, which includes terrestrial and extra-terrestrial rock-forming materials [9]. Hence, its composition and structure resemble those of moons and other celestial objects where pyroxenes are expected to be rather prominent [10]. Similar experiments as the ones described were already carried out and analysed in, e.g. [11–13].

This thesis aims to give a detailed overview of the recent adjustments made to the experimenting apparatus by comparing data obtained by different measurement cycles. To perform these experiments, the quartz crystal microbalance (QCM) technique was used, which allows for very precise measurements of mass changes in real time and *in situ*. Enstatite was used for the production of two target types that were irradiated during the experiments described in this thesis. A quartz coated with a thin mineral film via the pulsed laser deposition (PLD) technique was investigated as well as a pellet consisting of ground and compressed enstatite. A second QCM is used for collecting the sputtered particles and is therefore referred to as the catcher QCM. The sputtering yields of Ar^+ and He^+ ions were measured for both targets so that the QCM irradiations served as a reference for the pellet measurements. During the experimental process, the beamline underwent multiple technological improvements, which eventually enabled the measurements with helium ions.

1.2 Sputtering

The term sputtering describes the removal of particles from a solid's surface due to bombardment by ions with energies in the range from eV to MeV [14]. When an incoming ion hits the target, it scatters multiple times at target atoms on its way through the material. With each collision, it transfers a part of its momentum and energy onto the respective target particle. If enough momentum pointing out of the surface is transferred to one such particle, its binding energy to the surface is overcome and it leaves the solid permanently [15]. A fully detailed description of sputtering can be found in [16].

When it comes to evaluating experimental data, a key quantity is the so-called sputtering yield Y. It is defined by:

$$Y = \frac{\text{number of sputtered particles}}{\text{number of incoming ions}} \tag{1}$$

The sputtering yield is a statistical quantity that gives information on how many target particles are sputtered, on average, per incident ion. It depends heavily on both target and projectile properties. These include, but are not limited to, projectile energy, mass and angle of incidence as well as the mass of the target atoms and their binding energies to the surface [14]. Figure 1 shows a typical dependency of the sputtering yield on the impact angle for a flat sample. The angular values are typically measured with respect to the surface normal of the target so that an angle of incidence $\alpha = 0°$ describes normal incidence. When bombarding the target at low angles, a large fraction of the incoming ion momentum is directed into the surface, where a collision cascade is initiated. The probability of target atoms colliding in such a way that their momentum is reversed is comparatively small and as a result, less sputtering occurs. When the angle of incidence is increased, the incoming particles possess a momentum component parallel to the surface. As a consequence, the collision cascade evolves closer to the surface and target atoms are more likely to get ejected from the target material, thus the sputtering yield increases. When the angle of incidence grows even bigger, a larger proportion of the projectiles will be reflected by the surface until the point where no sputtering occurs. The sputter yield usually reaches its maximum at an angle of around 60°-70° with respect to the surface normal.

Usually, the dominant means of sputtering is *kinetic* sputtering, where an incoming ion collides with multiple target atoms, to which some of the projectile's momentum

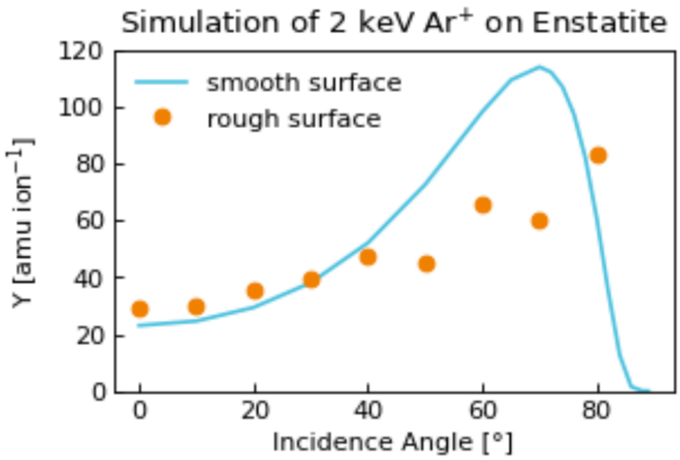

Figure 1: Typical angular dependency of the sputtering yield. The blue curve follows a simulation of a smooth surface by SDTrimSP, whereas the orange dots represent the surface of an enstatite ($MgSiO_3$) pellet. These data points are calculated by a code that considers geometric aspects of the sample [17]. Image taken from [18].

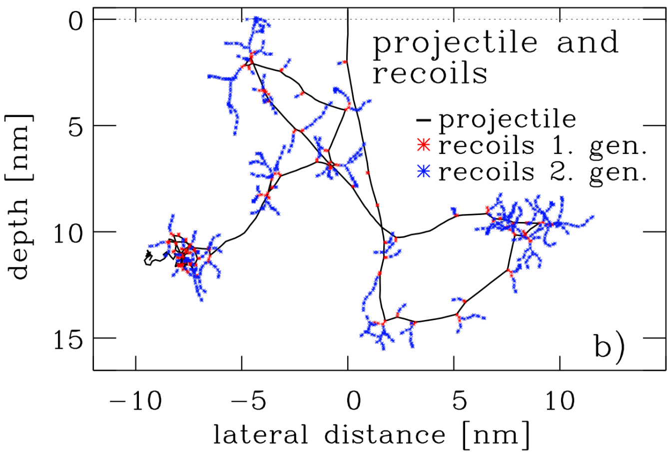

Figure 2: An example of a collision-cascade as simulated by the binary collision approximation software SDTrimSP for 2 keV He^+ atoms impinging perpendicular on a Ni target. The black lines represent the trajectory of the He atoms whereas the red and the blue dots represent Ni recoils of the first and second generation, respectively. Image taken from [15]

is transferred. Subsequently, these atoms themselves set in motion further recoils in the material and thus a so-called collision cascade is formed. Figure 2 shows such a collision-cascade as simulated by the binary collision approximation (BCA) software SDTrimSP. It is important to note that only after several collisions a target particle will receive enough momentum pointing out of the surface to overcome its surface binding energy. This suggests that a minimum kinetic energy is needed for an ion to eject a target particle out of a solid's surface. Besides these purely kinematic considerations, there exist also other kinds of sputtering effects.

When performing irradiation experiments with multiply charged ions, *potential* sputtering effects can become apparent. These are mainly observed in semiconducting or insulating materials [19]. When a higher charged ion approaches the target, it is accelerated towards the surface due to its own image charge. Additionally, target electrons will be ejected from the surface towards the incoming ion in order to compensate for its charge, which leads to the formation of a highly excited hollow atom. This is a multiply-excited neutral atom, which carries a vast proportion of its electrons in higher than usual energy levels so that the inner shells remain mostly empty [20]. These so-called Rydberg states then decay by emission of electrons and photons, which are able to interact with the surface causing additional sputtering effects among other processes. The resulting sputtering yields strongly depend on the ion's charge state. This enables sputtering to take place even at impact energies well below the kinetic energy threshold [19]. All experiments described in this thesis were conducted with singly charged ions so that potential sputtering effects could be neglected for data evaluation.

The irradiation of a solid's surface with energetic particles causes a variety of particles to be ejected. For multi-component targets, the different particle types are not distributed stoichiometrically during the initial phase of the bombardment. It was observed in past experiments that lighter particles are more likely to be emitted from the surface than heavier ones, which leads to a disproportionate amount of heavy components in the solid [21]. This effect is known as *preferential* sputtering and causes the distribution of the sputtered particles to differ from the original surface composition. For projectiles with energies in the vicinity of keV and a fluence of around 7×10^{15} ions cm^{-2} it takes less than 1000 s until a steady state is reached. After this time period, the emitted particle flux was found to be identical to the solid's bulk composition [21].

Channelling is observed when an ion penetrates a crystalline medium under a low angle of incidence with respect to certain lattice directions. If this is the case, the impinging ion is partially constrained to move in the open spaces of the crystal's lattice. This reduces the likelihood of the ion colliding with crystal atoms in such a way that a collision cascade is initiated. As a consequence, the structural damage on the crystal is significantly reduced, while a sharp increase in the average penetration depth of the ions is observed in these directions. To a certain extent, this is also the case with the experiments conducted on the mineral bulk sample. The critical angle under which channelling occurs grows with a reduction in ion energy and is very sensitive to the charge state of the projectiles and the substrate atoms [22]. Channelling influences the penetration depth distribution of the incoming ions and the number of displacements per atom, which has to be accounted for during experiments.

Conducting experiments on any kind of sample with a non-ideally flat surface causes a variety of phenomena to occur. In general, the sputter yield mainly depends on the location where the ion collides with the target and it is only weakly correlated to the global angle of incidence. Instead, one has to average over the whole target area since the roughness of the sample is statistically distributed. As is shown in figure 3, the local angle of incidence changes drastically with the local roughness features of the surface (A) [23]. Shadowing takes place when an area on the surface is protected from ions with a certain angle of incidence due to the roughness of the surrounding area (B). Depending on the local angle of incidence ions can also get reflected by the surface and in some cases cause little to no sputtering at all. An atom can also be ejected from the surface under such an angle that it hits the target at a different location, where it causes secondary sputtering. This usually occurs at higher angles of incidence and is not limited to rough surfaces only (C). However, the majority of ejected particles do not possess the energies necessary and can become re-deposited in the material instead, therefore not contributing to the total sputtering yield (D) [24]. As a result, the theoretical description of sputtering becomes rather complex.

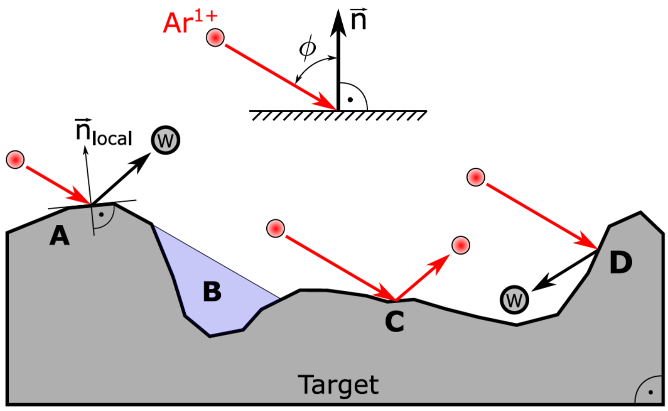

Figure 3: Depiction of the different sputtering effects that are observed in correlation with surface roughness for ions impinging on a solid under the angle of incidence ϕ to the surface normal; A: Local angle of incidence deviates from ϕ; B: Shadowing; C: Reflection of the projectile; D: Re-deposition of sputtered particle. Image taken from [25].

2 Methods

2.1 Quartz Crystal Microbalance (QCM) Technique

The quartz crystal microbalance (QCM) technique is a well-established experimental method at the Institute of Applied Physics (IAP) [26] since it has proven to be a reliable tool for determining small mass changes in the order of pg/s. These measurements are performed in real time and *in situ*.

In order to perform measurements using the QCM technique, a SC-cut quartz is covered with gold electrodes. Applying an AC voltage excites the quartz to a shear mode thickness oscillation in its so-called eigenfrequency, which can be measured with great precision. When irradiating the quartz with an ion beam, two major effects are observed. On the one hand, a portion of the incoming ions is implanted into the resonator. On the other hand, sputtering of surface atoms takes place. Both of these phenomena lead to changes in the quartz's overall mass, which carries over to its resonance frequency. By monitoring this frequency during experiments, it is possible to calculate this mass change according to the Sauerbrey equation [27]

$$\frac{\Delta f}{f_Q} = -\frac{\Delta m}{m_Q}, \tag{2}$$

where m_Q and f_Q represent the quartz's initial mass and frequency, respectively. Δm and Δf describe the changes therein per time span Δt. It is useful to employ the Sauerbrey equation to express the difference in mass in terms of mass change per unit area Δm_A as

$$\Delta m_A := -\frac{\Delta m}{A_Q} = \frac{\Delta f m_Q}{f_Q A_Q} = \frac{\Delta f_Q d_Q}{f_Q}, \tag{3}$$

with A_Q being the surface area of the quartz, d_Q its thickness and ρ_Q its density.

This expression alone is not sufficient to determine the sputtering yield Y, which is defined as the average number of sputtered target atoms per impinging particle on the target. To calculate this property, it is necessary to know the number of projectiles hitting the target per unit area during the time span Δt. Provided that the beam current density, denoted as j, remains constant during measurement, one can express this number by

$$N_i = \frac{j\Delta t}{qe_0}, \tag{4}$$

where q represents the charge state of the ion and e_0 the elementary charge, respectively. To obtain the mass change per impinging ion one has to divide the mass change per unit area Δm_A by the number of incoming particles N_i, which is shown in the following equation:

$$y_T := \frac{\Delta m_A}{N_i} = -\frac{\Delta f \rho_Q d_Q}{f_Q} \cdot \frac{qe_0}{j\Delta t} = -\frac{\Delta f}{\Delta t} \cdot \frac{1}{j} \cdot \frac{\rho_Q d_Q q e_0}{f_Q} \tag{5}$$

This equation can be separated into three major parts. The first expression $\frac{\Delta f}{\Delta t}$ denotes the slope of the recorded frequency curve over time, which can be extracted from the frequency data. For calculating the second term $\frac{1}{j}$ it is necessary to know the beam current density. This is achieved by measuring the ion current before and after each measurement using a Faraday cup (FC). The last term in (5) consists solely of constants, which can be taken either from literature or are known through the manufacturer of the QCM. Hence, it is possible to obtain the mass change per impinging ion by experiment.

One important fact when using a quartz crystal microbalance is that the quartz's sensitivity is not distributed evenly across its surface area [27]. As has been shown at the IAP, its sensitivity distribution is best approximated by a Gaussian function whose free parameters have been determined in past experiments [28, 29]. Since the Sauerbrey equation only remains valid for homogeneous mass removal across the quartz's surface area, one has to ensure that the ion beam is distributed evenly before hitting the target. This is achieved by the use of scanning plates at the entrance of the experimentation chamber to which a triangular AC voltage of 52 Hz and 1.6 kHz is applied in y- and z-direction, respectively [30]. By varying the amplitude of these voltages the beam's cross-section can be modified.

2.2 Catcher QCM Configuration

As described in the previous section the QCM technique enables measurements of mass changes on an atomic scale. However, not every material is suited to be applied to a quartz as a coating. Especially with compound materials like enstatite ($MgSiO_3$) there are certain technological limitations when it comes to reproducing the material's roughness and crystallinity as a thin film. To circumvent this particular problem, the so-called catcher QCM setup was developed. A second QCM is introduced, which serves the purpose of collecting the sputtered target particles during measurements. These particles are deposited on its surface and increase its overall mass. As is the case for the primary QCM, these changes in mass affect its resonance frequency. This new setup does not allow for direct measurements of the sputtering yield, but it enables its calculation through the changes in mass of the catcher QCM. It also enables more flexibility when choosing the target material, since the catcher is indepent from the irradiated target.

The catcher QCM is installed in a radially symmetric position relative to the target, which is outlined in figure 4. This ensures that the distance between the target and centre of the catcher QCM remains constant at all times independent of the catcher's position. This is important since the flux density of the sputtered particles decreases radially proportional to $\frac{1}{r^2}$. A servo motor enables the catcher to perform circular movements around the centre axis of the target holder. The whole process is mostly automated so that the catcher can be moved to different angles during measurements to provide information about the angular distribution of sputtered particles at each particular location relative to the target. An outline of the catcher QCM setup is shown in figure 4. All catcher angles are defined with respect to the target surface normal so that they can be easily compared when analysing data from different angles of incidence. During measurements, particles will be ejected from the target's surface area where they might collide with the catcher QCM. The typical energies of sputtered particles lie below 50 eV, which prevents them from inducing sputtering on the catcher QCM themselves and instead allows some of the particles to remain stuck to the catcher's coating [31].

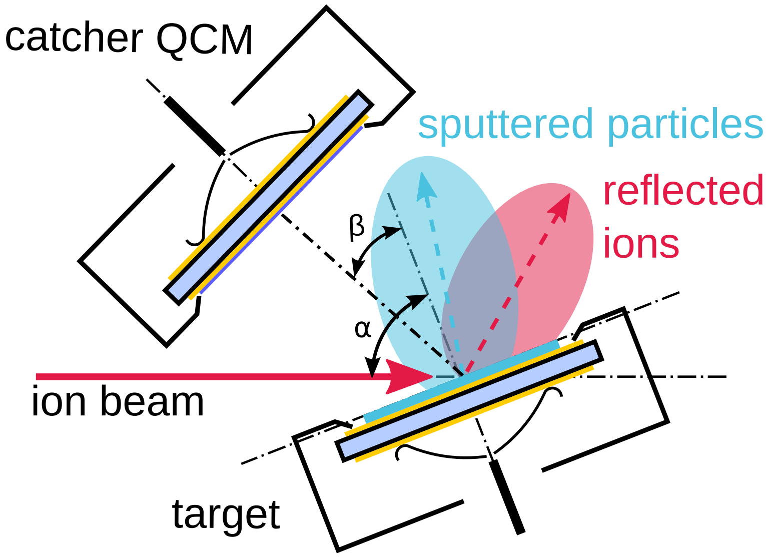

Figure 4: Overview of the catcher QCM setup. The ion beam impinges on the target under an angle of incidence α with respect to the surface normal. The light red and light blue areas represent the angular distributions of the reflected projectiles and the sputtered particles, respectively. The catcher holder is located at an angle of β and can perform circular motion around the centre of the target. Image adapted from [32]

It is important to note that introducing a second quartz crystal microbalance to the setup also demands more cautious data evaluation. First of all, the sticking coefficients to the catcher QCM are not constant over time since the gradual accumulation of particles alters its coating during experiments. Secondly, ions might be reflected from the target's surface directly to the catcher where they can either be implanted or cause sputtering to occur. Lastly, the QCM's sensitivity is not distributed uniformly across its surface as was already mentioned. In addition to that, the catcher signal is usually about ten times lower than the corresponding signal measured on the target [28].

The signal of the primary QCM is not affected if material of the target holder is sputtered during an experiment. This is not the case for the catcher QCM, however. Since it can not distinguish between different materials it is necessary to confine the ion beam to a certain area on the samples so that it does not hit the target holder. As a consequence, every single ion contributes to the catcher signal and therefore the total number of ions needs to be determined. Hence, equation (4) needs to be modified. The number of incoming ions per unit area has to be replaced by the total number of impinging ions. The same applies to the mass change per unit area. One is now left with

$$N_i^{total} = \frac{I\Delta t}{qe_0} \tag{6}$$

and the catcher mass change per ion corresponding to

$$y_C := \frac{\Delta m}{N_i^{total}} = -\frac{\Delta f}{\Delta t} \cdot \frac{1}{I} \cdot \frac{\rho_Q d_Q q e_0 A_Q}{f_Q}. \tag{7}$$

Here the ion current density j is replaced by the total ion current I, while the area of the catcher QCM is denoted by A_Q. Since a bigger catcher area would result in an increase of the overall signal while the number of sputtered particles from the target does not change it is reasonable to define the mass change on the catcher per ion and solid angle $y_{C,\Omega}$ as follows:

$$y_{C,\Omega} := y_C \cdot \frac{1}{\Omega} \approx \frac{\Delta f}{\Delta t} \cdot \frac{1}{I} \cdot \frac{\rho_Q d_Q q e_0 A_Q}{f_Q} \cdot \frac{r^2}{A_Q} = \frac{\Delta f}{\Delta t} \cdot \frac{1}{I} \cdot \frac{\rho_Q d_Q q e_0 r^2}{f_Q}. \tag{8}$$

Here, r describes the distance between target and catcher. Note that this equation does not depend on the quartz's area anymore. Thus, data resulting from different setups can be compared more easily. Given that the distance $r = 17$ mm and the diameter of the quartz $d_Q = 7$ mm [28] for the presented setup one can calculate Ω to be

$$\Omega_C = \frac{A_Q}{r^2} \approx 0.133\,\mathrm{sr}. \tag{9}$$

It seems at first sight that equations (5) and (7) have opposite signs. This is compensated by the fact that $\frac{\Delta f}{\Delta t}$ is positive for the target quartz since mass is lost during irradiation and it is negative for the catcher due to its increase in total mass. Hence this is a more convenient notation to compare the two properties.

3 Experimental Setup

3.1 Beamline

All experiments described in this thesis were conducted with an ion beam produced by a 14.5 GHz electron cyclotron resonance (ECR) ion source named SOPHIE at the Institute of Applied Physics (IAP) at the TU Wien. In such an ion source a plasma is confined by a superposition of two magnetic fields. The axial magnetic mirror field is produced by a permanent magnet, whereas the radial field is generated by a permanent magnet hexapole. Electrons are excited to perform cyclotron motion via microwave radiation, whose frequency corresponds to the gyromotion frequency of the electrons. This causes the electrons to collide with the of particles of the working gas, resulting in electron impact ionisation and the ignition of a plasma. Multiply charged ions are predominantly produced via sequential electron impact ionization [33]. The ions can then be extracted from the plasma and are accelerated by applying a potential of up to 6 kV, which is sufficient for solar wind energies of 1 keV/amu for hydrogen and helium, the elements most prominent in the solar wind [7]. A more detailed description of the ion source can be found in [33] and [34].

After extraction, the ions pass two separate quadrupole magnets, which are used to focus the ion beam. A sector magnet ensures that only ions with the desired mass over charge ratio make their way into the beamline. An aperture and a Faraday cup (FC) are installed at the entrance of the beamline, which allows for current measurements right after the sector magnet. To gain an overview of what species the ion beam consists of, a spectrum can be taken by measuring the ion current in the FC while continuously increasing the magnetic field strength of the sector magnet. To maximise the current into the FC the strength of both quadrupole magnets and the sector magnet needs to be adjusted repeatedly. Once the optimal settings for a given m/q ratio are found the Faraday cup is removed. A first set of deflection plates is located directly after the FC. If turned on, a voltage is applied to the plates. This causes the ion beam to bend sharply, thus preventing it from entering the experimentation chamber. This mechanism enables remote control of the ion beam and is frequently used both during sample preparation and the measurement process itself. In case the deflection plates are switched off, the ion beam passes through two sets of ion optics, each consisting of two pairs of electrostatic deflection plates and an einzel lens. Between those two sets, another aperture is installed which is connected to a picoamperemeter. When measuring the ion current on the apertures one can adjust the beam's trajectory through the deflection plates so that a minimal proportion of the ions hit the aperture. This ensures that the beam is focused sharply and also provides information about its intensity. When the beam enters the experimentation chamber, it passes through a set of scanning plates whose purpose it is to widen the beam profile. By applying saw-tooth voltages, the beam is scanned over a rectangular area. This scanning area can easily be modified by altering the voltage amplitudes applied to each pair. An overview of the beamline setup is shown in figure 5.

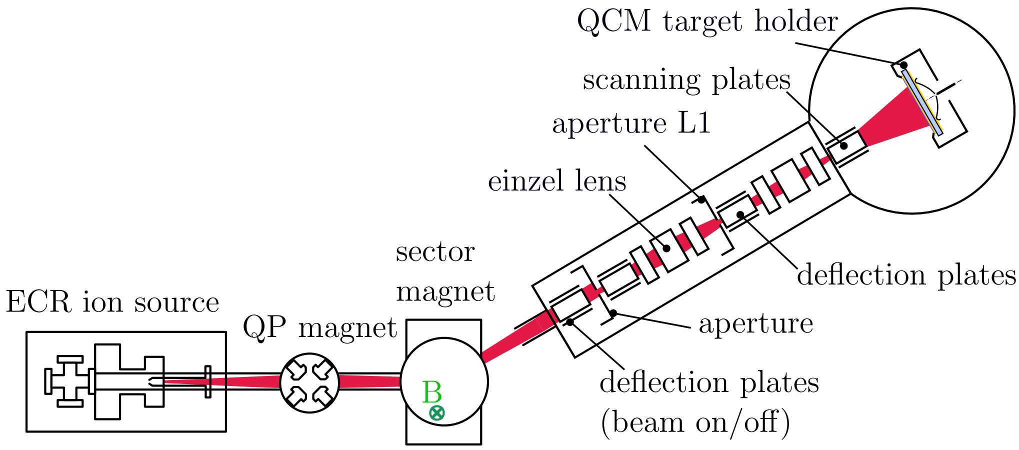

Figure 5: Basic scheme of the beamline which was used to conduct the experiments described in this thesis. After exiting the ECR ion source the beam passes two quadrupole magnets as well as a sector magnet. After the right m/q ratio has been selected the ion current travels through two sets of ion optics until it passes the final scanning plates at the entrance of the experimentation chamber. Figure adapted from [35].

3.2 Experimentation Chamber

The experimentation chamber hosts the target holder, the catcher QCM and an electron floodgun. The target holder is mounted on an $xyz\phi$-manipulator and is divided into three main compartments. The topmost device is a Faraday cup which is used to measure the ion current beam density before and after each measurement. The middle part holds the target QCM, also referred to as primary QCM. It is fixed to the stainless steel target holder via a tungsten spring and it is coated with a thin film of enstatite. Gold electrodes provide the electrical connections necessary for the quartz to be excited in its resonance frequency. Beneath the quartz, an enstatite pellet is installed. Both the pellet and the quartz are equipped with heating wires and a K-type thermocouple to be able to conduct measurements at different temperatures and for heating as a part of sample preparation. A 3D rendering of the target and catcher holder is displayed in figure 6. As was already described in section 2.2, a catcher QCM setup is necessary to measure the mass removal per incoming ion for the pellet since there is no inherent frequency data available.

The purpose of the floodgun is to avoid the accumulation of positive charge on the targets during measurements. This is especially necessary for pellet irradiations as it is an insulating mineral bulk. By emitting low-energy electrons into the chamber from a filament the pellet can be kept charge neutral. Without the floodgun, a positive charge would build up on the pellet, which would cause incoming ions to be repelled. This would lead to deceleration and deflection of the projectiles and cause them to hit the target holder instead of the samples. As a result, the target holder material would be sputtered instead of the desired target material. However, this process was shown to be unnecessary for QCM irradiations [13]. On a thin film of wollastonite ($CaSiO_3$)

only a voltage of up to some 10 V was estimated to build up, which is negligible compared to the kinetic energies of the incoming ions, which lie in the vicinity of several keV. Since the thicknesses of wollastonite and enstatite films are roughly the same this relation holds also for the experiments performed in this thesis.

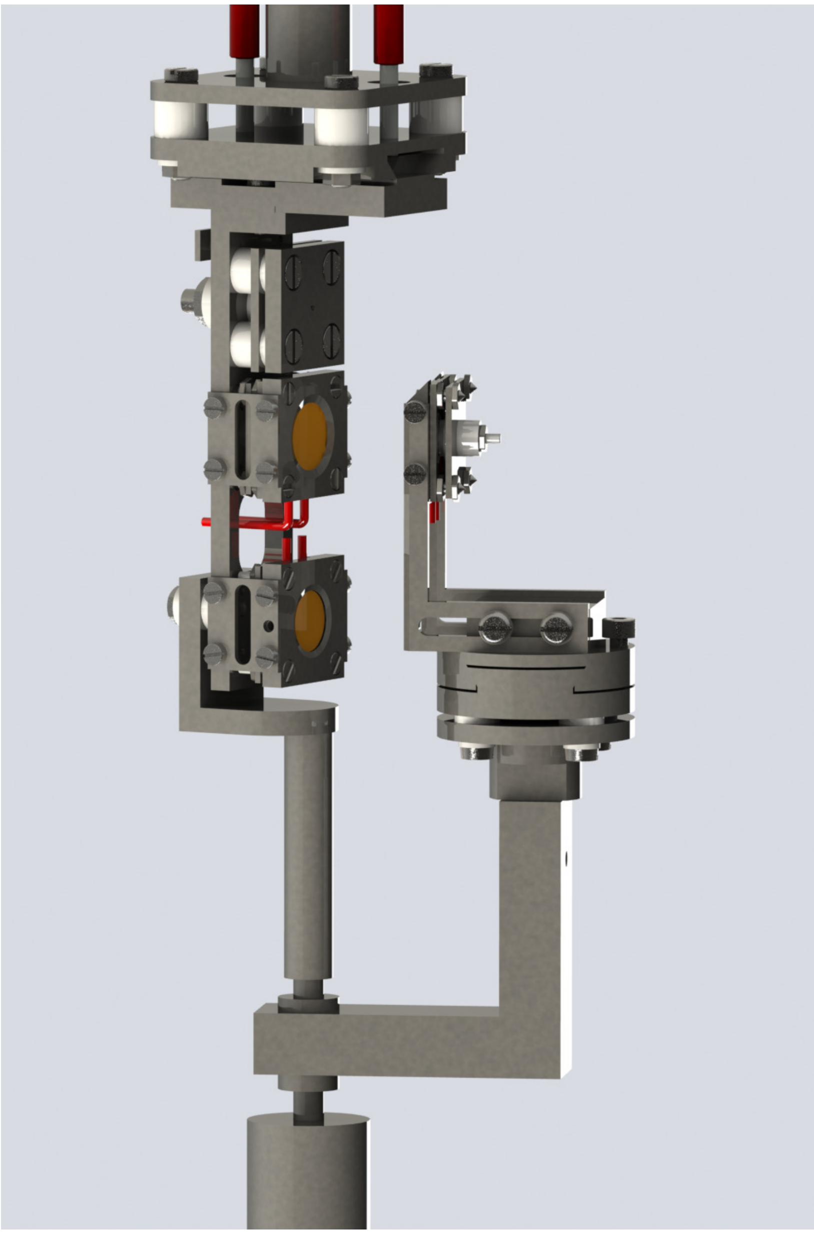

Figure 6: 3D model of target and catcher holder. A Faraday cup (FC), the primary QCM and the pellet are mounted on the sample holder from top to bottom. The heating wires of the samples are represented in red. The insertion tube as well as the catcher holder's rod can be seen at the bottom of the constellation.

The target holder is mounted on an $xyz\phi$-manipulator which is connected to servo motors. This enables the target to move in all spatial directions as well as to rotate around its centre axis, which determines the angle of incidence when performing measurements. The setup also allows for automated switching between pellet and QCM position. This is achieved by moving the target holder up and down during measurements while the catcher remains in the same position. The catcher holder is located beneath the targets and contains only one QCM. When there is no measurement in progress, the catcher usually rests in a parking position at the very bottom of the chamber to avoid collisions between catcher and target holders. It is mounted on an $xyz\phi$-manipulator too. Unlike the target holder, movements of the catcher in the x, y and z directions are currently not remote controlled and its alignment has to be adjusted manually. Only its angular position is set by a stepper motor. This is necessary to achieve a high degree of automation during measurements. To investigate the angular distribution of sputtered particles for different angles α, as is indicated in figure 4, the catcher is automatically rotated to the desired angle β set by the experimenter between the irradiations. The catcher holder itself is mounted on a stainless steel rod, which has to be inserted carefully into the target holder's tube before each measurement. In an effort to minimise geometric uncertainties, the insertion tube of the target holder was prolonged and its diameter reduced to decrease the leeway of the catcher rod inside the tube. Also, powdered MoS_2 was used as a lubricant to reduce friction between tube and rod. Figure 7 shows both catcher and target holder during a typical catcher QCM cleaning procedure as described in section 4.2, where no insertion of the rod into the tube is needed.

It is of importance that the radial symmetry between catcher and target holder persists throughout each measurement to ensure that the acquired data are comparable to past or future measurements. This has been an issue in the past, which was already addressed in a project report [36]. In former experiments, there have been significant discrepancies between catcher QCM signals of different measurement series. These variations were attributed to the geometry of the setup. Since then, many adjustments were undertaken in an effort to solve this problem, none of which resolved the issue. However, as a part of this thesis, the setup has been improved further not only by modifying its geometry, but also because of the introduction of a new catcher preparation method, which is discribed in section 4.3.

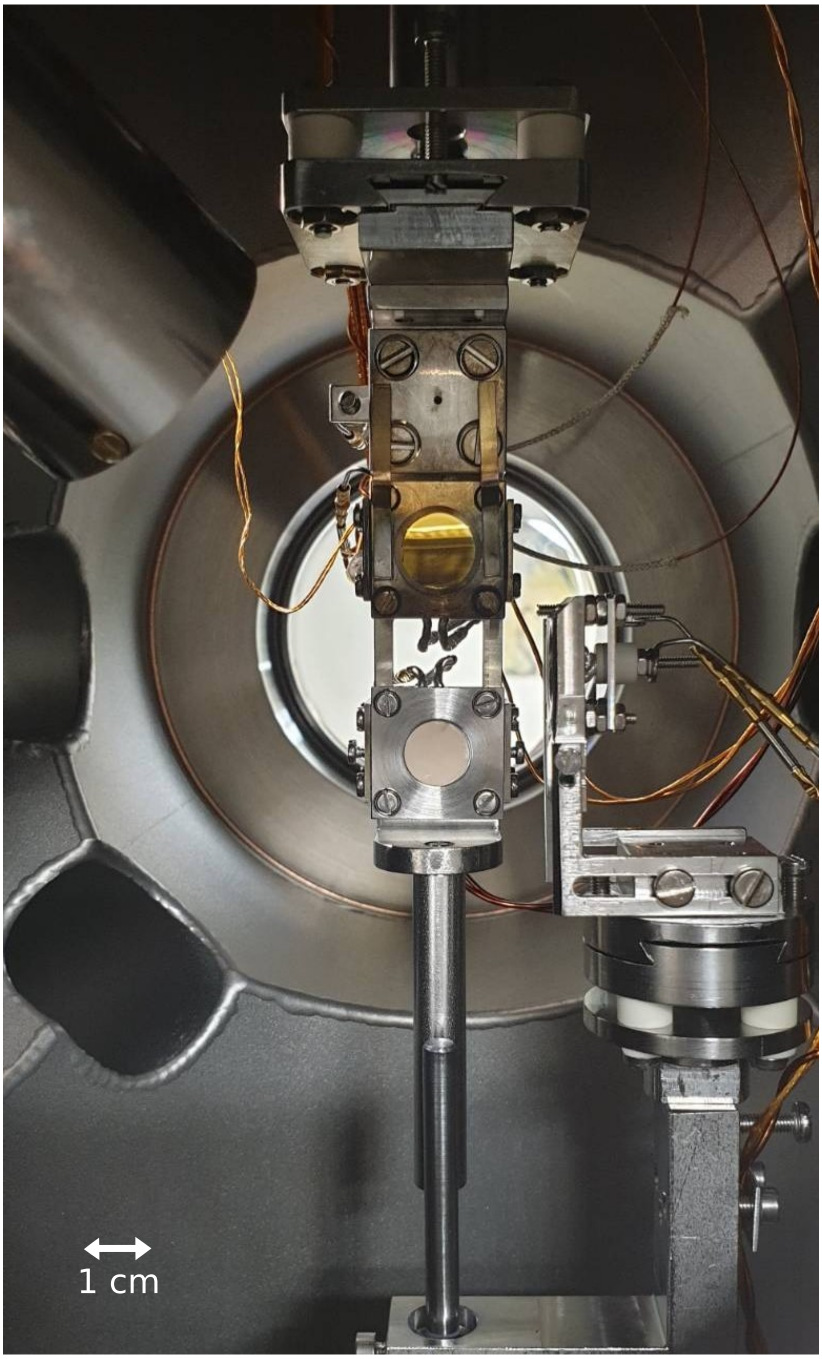

Figure 7: Picture of the target and catcher holder inside the experimentation chamber. The Faraday cup is located at the topmost position on the target holder. The primary quartz is installed beneath. The compartment on the bottom holds the enstatite pellet. The catcher is located to the right of the target holder. Catcher rod and insertion tube can both be seen at the bottom of the image.

3.3 Controlling of the Catcher Eigenfrequency

In the past, the catcher QCM used to be controlled by a Python script that excited its first and third eigenfrequency mode quasi-simultaneously. This was achieved by alternating between the frequency measurements of each mode, which resulted in reduced accuracy. To improve the frequency resolution the catcher ground mode oscillation was driven using an analog oscillator whose output was monitored using a frequency counter and a LabVIEW program [37]. Frequency measurements were taken once per second, with an integration time of 10 ms. Since LabVIEW is a commercial software it requires an active internet connection upon startup to verify the licence. However, the personal computer (PC) was not connected to the internet to eliminate the risk of possible interruptions due to maintenance or updates of the operating system. Because of the aforementioned reasons, a transition from LabVIEW to a home-made controlling tool was desired. As a part of this thesis, a graphical user interface (GUI) was introduced using the Python programming language [38]. The GUI receives the frequency values of the catcher QCM directly from the Tektronix Frequency Counter FCA3100, processes the data and displays it in a user-friendly manner. This led to a five times better time resolution of the QCM's signal compared to the initial Python controlling script. Additionally, the noise of the frequency signal could be reduced from around 10 mHz to less than 2-3 mHz. This improvement is particularly important since the signal of the catcher QCM is inherently small compared to the primary QCM [32].

Another feature of the GUI is the newly introduced spike filter. When measuring the frequency of the quartz nonphysical data points are observed on a regular basis. Since these signals oftentimes deviate from the usually measured frequencies by an order of magnitude they lead to a distortion of the visualisation. To solve this issue the Python code was adapted to filter these so-called spikes and simply replace them with the previous frequency value. The filtered frequencies are stored in a separate output file so that no information is lost in the process. The exact locations of these replacements are displayed as red dots on the graph for the user to see. This modification improved the program greatly since it became much easier to depict the changes in frequency visually, thus saving time and effort for the user. Figure 8 shows the basic structure of the spike filter.

The program starts off by reading the frequency data from the Tektronix frequency counter (FCA3100) and initialising two arrays, f and s. f stores all the data points for plotting (A), whilst s is used as a so-called spike-array to save the nonphysical data points (B). Once the program reads in a frequency f_i, it is compared to the previous value f_{i-1} (C), given that there is one. In the next step, it is reviewed whether the difference between the two values exceeds a certain threshold x (D). This threshold dictates the maximum frequency step size tolerated by the program. If this limit is not exceeded, the latest frequency value f_i is stored in a data array for plotting f and it moves on to the next data point (E). This is the simplest case in which nothing special happens. However, if the threshold is exceeded, the code investigates whether the two previous frequency data points f_{i-1} and f_{i-2} are identical (F). If they are the program knows that they were replaced in the previous cycle. If not, the most recent frequency

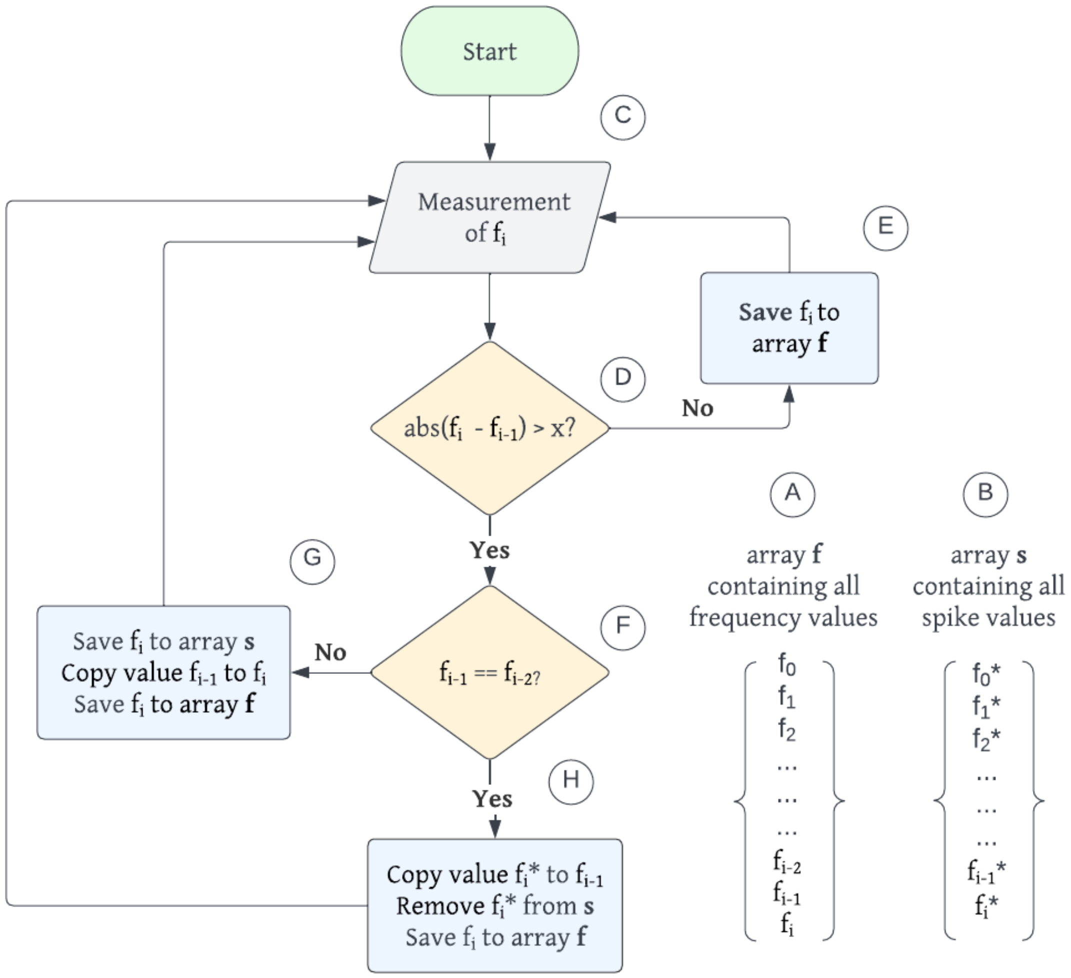

Figure 8: Flowchart of the code section, which is responsible for filtering nonphysical data points during frequency measurements of the catcher QCM. The two arrays located to the right of the image are used to store the regular frequency data (A), as well as the frequency values of the replaced spikes (B).

value f_i is stored in a spike array s and the last element f_{i-1} of the frequency array f is duplicated to fill the vacant spot (G). This way it is guaranteed that the frequency curve continues smoothly. Afterwards, the program investigates the next data point and starts comparing again.

The aforementioned program performs very well when it is asked to remove one spike at a time. Oftentimes, when the catcher is rotated, however, there is a one-time shift in resonance frequency. Usually, this shift exceeds the threshold and has to be accounted for by the program. Such a shift can be regarded as many spikes that occur in sequence. As already mentioned, a reliable way for the program to identify consecutive spikes is to check whether the last two frequency values f_{i-1} and f_{i-2} are identical, before saving f_i. Since the usual resonance frequencies of the catcher QCM lie in the vicinity of around 6 MHz, it is highly improbable that two consecutive frequency measurements result in the exact same value. In addition, the program only detects two floats as truly identical if they have been set to the same numerical value. If a shift is observed, the previously copied frequency value f_{i-1} in f is replaced by the "spike" value f_i^*, which is then removed from s (H). This way the at first substituted spike is restored and the program continues a new loop. Complicated though step H may seem, it is necessary to handle frequency jumps properly such that they are not unintentionally filtered away. Figure 9 shows a screenshot of the resulting global and local plot windows as displayed by the interface. A more detailed description of the GUI can be found in [39].

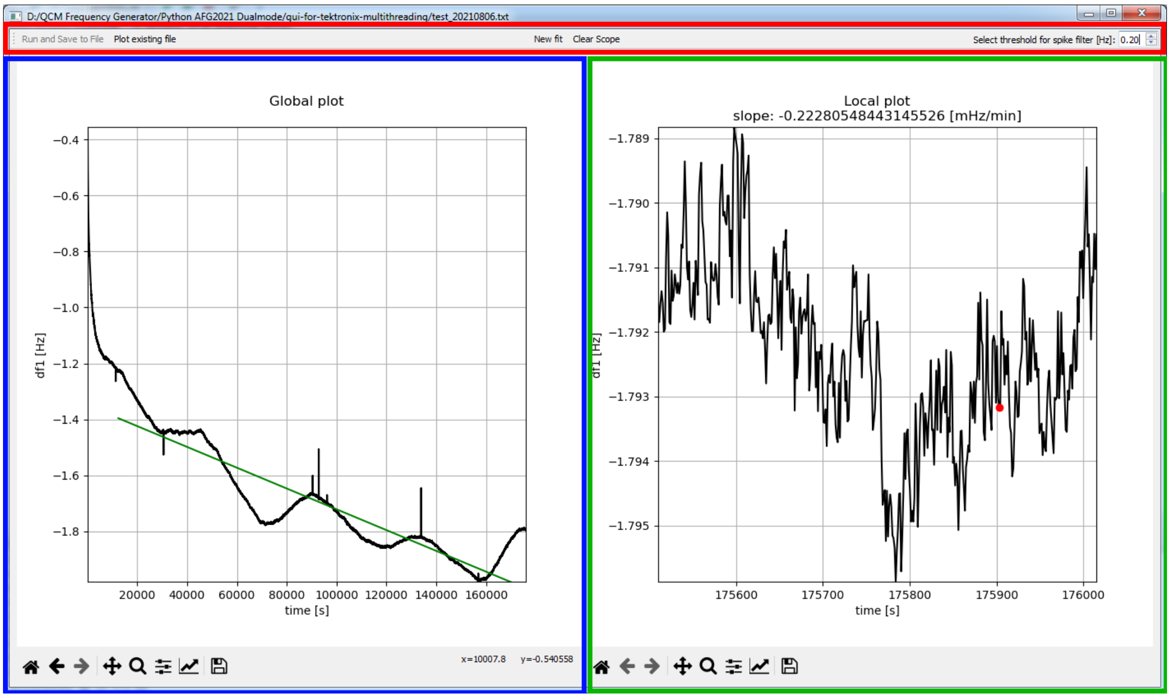

Figure 9: Screenshot of the FCA3100 control GUI. A global frequency curve is displayed on the left display, whilst the right part of the interface shows only the last 500 seconds of measurement. A red dot is displayed in the local plot at the location where a spike was filtered.

4 Sample Preparation

4.1 Production Process of the Samples

The thin layer of enstatite was applied to the surface of the quartz crystal microbalance via pulsed laser deposition (PLD) at the Institute of Chemical Technologies and Analytics at TU Wien. This is achieved by the use of a 248 nm KrF excimer laser with a pulse frequency of 5 Hz and a pulse energy of 400 mJ/pulse while maintaining a target temperature of 250°C [36]. The wollastonite samples used in former experiments also followed the same production process [11, 12, 40]. The produced layers underwent detailed analysis by Rutherford Backscattering Spectrometry (RBS) as well as Time-of-Flight Elastic Recoil Detection Analysis (ToF-ERDA) [12]. These procedures revealed the depth-dependent composition of the layers as well as their thickness. It was concluded that indeed a layer of enstatite stoichiometry had formed. It is important to note, however, that this film is amorphous and has a smooth surface. Due to its lack of crystallinity, it is not well suited for providing realistic sputter yield data in the context of the erosion of planetary surfaces.

To observe the influence of roughness and crystallinity on sputtering behaviour it is necessary to perform irradiation experiments on a mineral pellet, which represents a more accurate approximation of planetary surfaces. The enstatite pellets, which were used in the experiments of this thesis, possess a polycrystalline structure and were provided by the University of Bern. A special production process was necessary to manufacture these pellets with sufficient stability. Wollastonite ($CaSiO_3$) and enstatite are first ground in a RETSCH agate disk mill until the powder begins to agglomerate. Subsequently, a thin film of wollastonite is pressed onto the steel back plates as a base upon which the enstatite can be applied by using a pressure of 80 MPa. This procedure exploits the intrinsic adhesion of the mineral powders to the steel surface so that no glue or binder is necessary. A careful analysis of the pellet showed that both powder composition and the crystallinity of its grains were maintained during the manufacturing process. Additional information about the production and analysis of the pellet can be found in [41].

4.2 Cleaning of Target and Catcher

The most used method for cleaning samples during this thesis was sputter cleaning. A 2 keV Ar^+ beam is used to remove adsorbates and contaminants. The target QCM was cleaned under an angle of incidence $\alpha = 60°$ with respect to the surface normal while the catcher remained in parking position. For cleaning of the catcher QCM the target holder is rotated and moved out of the way (see figure 7 for the positioning of the target holder) so that the ion beam could pass through the chamber unhindered. Meanwhile, the catcher is moved to the height of the ion beam and rotated such that it faces the beam. In both cases, the ion beam is scanned over the total sample area. By measuring the resonance frequencies of catcher and target QCM the sputtering yields can be monitored during cleaning. Typically, a high sputter yield is observed in the initial phases of the cleaning procedure. This can be explained by the fact that adsorbates are only weakly bound to the QCM's surface and are therefore sputtered more easily. Once the sputter yield has stabilised the cleaning procedure is completed and the beam is turned off.

When it comes to cleaning the pellet, on the other hand, the sputtering yield cannot be measured. Instead, it is assumed that for similar contamination of pellet and QCM the same fluence is required for cleaning. As is the case for the primary QCM, the pellet is also cleaned under an angle of $\alpha = 60°$. Narrow scanning is used to guarantee that no material is sputtered from the target holder. The resulting surplus in flux is accounted for by a shorter irradiation time. The floodgun is activated to avoid the accumulation of positive charge on the pellet, as described in section 3.2.

An alternative cleaning procedure was investigated to minimise changes to the surface morphology and structure. Firstly, the target is heated through heating wires. The current through these wires was slowly ramped up to 4 A and was maintained constant for 6000 s before it was ramped down again. Through this heating cycle, a change of the primary QCM's resonance frequency of almost 20 Hz could be achieved, which suggests that material must have been ejected from its surface. Secondly, the floodgun was activated to irradiate the target QCM with 20 eV electrons to achieve even better cleaning results via ESD (Electron Stimulated Desorption) [42]. Finally, the target QCM was irradiated with ions afterwards. Almost immediately after starting the irradiation, the recorded sputter yield was constant, suggesting the almost total absence of contaminants. It is assumed that the pellet (for which no such direct confirmations exist) can be cleaned in the same manner, should ion bombardment not be desired.

4.3 PEP-C Procedure

As was discussed in previous projects the signal on the catcher QCM has been subject to transient effects like time dependencies of frequency data within and between measurements carried out at different points in time [36]. In the past, the setup was optimised in several ways, including fixing the geometry of the experiment and adaptations in the controlling of the involved QCMs. However, none of these approaches led to a solution of the issue.

Past experiments using an enstatite coated catcher suggest that its sticking coefficients might depend on the duration of the sputter cleaning procedure before each measurement. This explains why an individual coating forms before different experiments. It was also observed that catcher's signal strength varies greatly during one irradiation cycle which results in an unwanted time-dependency of the sputtering data [36]. To investigate this problem, a new approach was applied. To keep the setup as simple as possible, the enstatite-coated catcher QCM was replaced by a QCM with a film of only a single element. By focusing the ion beam on a pellet area that is not irradiated during experiments material can deposited on the catcher QCM without interfering with the actual investigations. The idea was to prepare the catcher in a steady state such that potential fluence-dependencies of ejecta sticking coefficients are eliminated prior to measurements. For this purpose, the catcher was rotated to $\beta = 25°$, where the most signal is expected, whilst the target was positioned in such a way that the Ar^+ ion beam impinges under an angle $\alpha = 45°$ relative to the surface normal. At this angle, a higher sputter yield is expected than at $\alpha = 0°$, but not as much geometrical distortion of the beam as at $\alpha = 60°$. Due to the beam's finite size, it is also important to limit its geometrical distortion to prevent steel of the target holder from being sputtered. The beam was therefore aimed at the topmost part of the pellet, 3.5 mm above its centre. Figure 10 shows a 2D outline of the pellet and its geometric dimensions. The red cross indicates the spot, which is used for focused sputtering. Since the topmost section is not irradiated during experiments, high fluences can be applied as possible changes in surface structure and morphology do not interfere with actual measurements. By dividing the beamtime during the coating procedure into shorter intervals, the coating process of the catcher QCM and the establishment of a steady state can be observed more conveniently. Additionally, potential drifts in resonance frequency can be compensated more easily for each point of measurement.

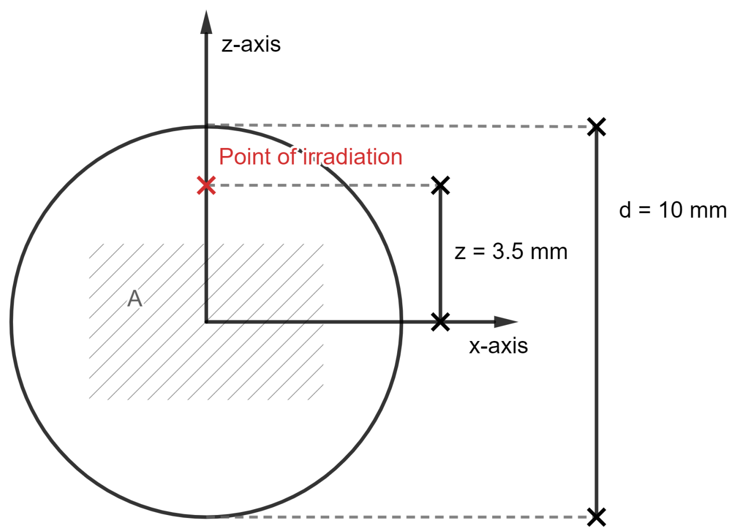

Figure 10: Outline of the pellet with a diameter of d=10 mm. The shaded area denoted as A is used for irradiation experiments when scanning is active. It was adjusted to fit the geometric distortion due to an incident angle of 45°. The red spot represents the point of focused irradiation to coat the catcher QCM before each measurement. It is calculated to be at z=3.5 mm above the center of the pellet so that only the unused pellet area is being irradiated.

During the development of this procedure, two different catcher QCM materials were investigated. Figure 11 shows the frequency slopes measured during a pre-coating procedure for two different materials of the catcher. The signals are calculated by subtracting the average slope of the two drifts before and after the irradiation from the measured frequency slope measured during ion bombardment. At first, an Au-Catcher was introduced into the system. Its signal, which is represented by the blue dots, was overshadowed by a factor of up to 5 by the thermal drift caused mainly by the floodgun. It is represented in the graph by the blue dots which scatter around zero with some of them being negative, which is unphysical. In a second attempt, a Fe-Catcher was tested since it was available at the laboratory at that moment. The following irradiations produced sufficiently high QCM signals which stabilised after only a few irradiations. The signals of the Fe-catcher are represented as orange dots. The dotted line shows the mean slope that was calculated for all irradiation slopes except for the first one. The shaded area marks a deviation of ±10% from this average, which is in the range of the otherwise expected experimental errors anyway. Following this measurement, the method was considered a success and it was subsequently given the name of Pellet Edge Pre-Coating (PEP-C) procedure. Measurements can now be performed under equal circumstances. After the experiment has finished the catcher QCM is cleaned until the sputtering yield is constant again. This state can easily be verified since the typical sputtering yield for iron is well known due to former research [43].

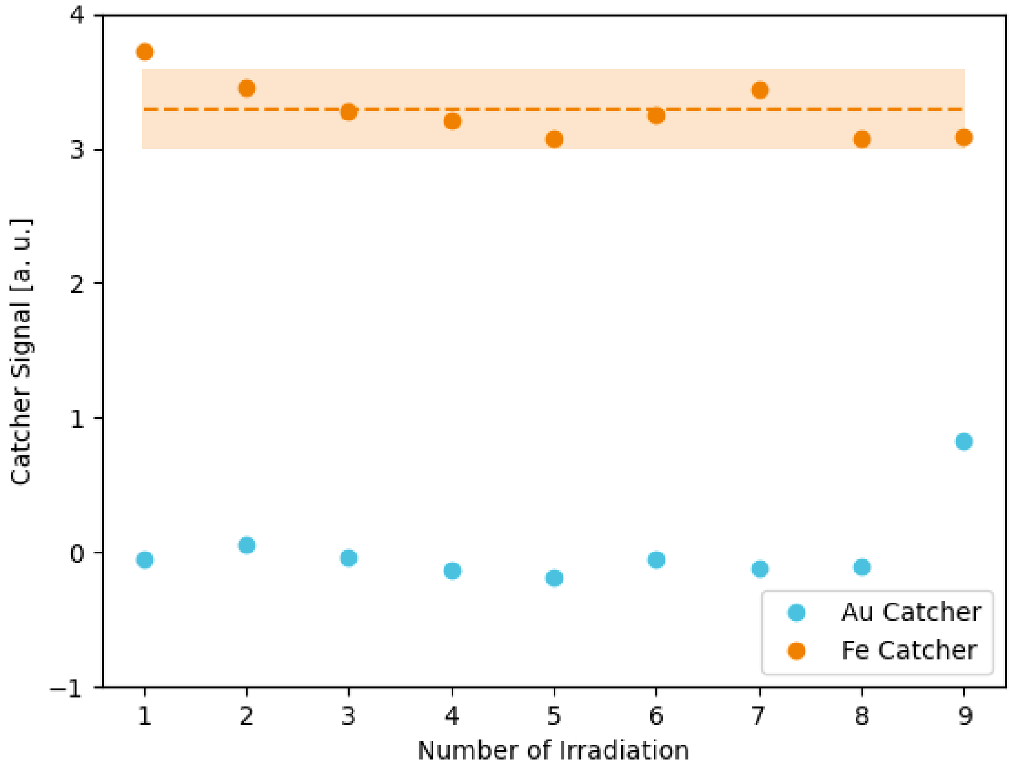

Figure 11: Comparison of the frequency slopes observed on both catcher QCMs during pre-coating. The blue dots represent the signal of the PEP-C procedure for the Au-Catcher whereas the orange dots show the frequency changes for the Fe-Catcher. The Au-Catcher produced very weak signals, which are overshadowed by thermal drift during the activation of the floodgun. The Fe-Catcher, on the other hand, maintained rather constant sticking coefficients throughout the irradiations. Both procedures were carried out using a 2 keV Ar^+ ion beam under $\alpha = 45°$ with respect to the surface normal. The catcher was positioned at $\beta = 25°$.

5 Measurements Process

5.1 Workflow

Before and after each measurement the profile of the ion beam was analysed to obtain information about the number of ions impinging on the target per time interval. Additionally, the quality of the beam's geometry can be reviewed. This presented a useful tool to determine whether the current had fluctuated since the start of the measurement. To create a beam profile the sample holder was positioned so that the beam is funnelled into the Faraday cup. The y- and z-position of the FC is then varied in 0.5 mm or 1 mm increments for narrow or wide scanning, respectively. The ion current is measured at each position. By interpolating through the data points an approximation of the beam's three-dimensional profile can be obtained, which is then used to calculate the integral ion current impinging on the sample [44].

In previous years there has been a clear tendency in the Atomic and Plasma Physics (APP) research group towards automating experimental procedures to maximise efficiency while simultaneously reducing the risk of human error. All measurements described in this thesis consisted of irradiating the targets in a certain order and moving the catcher automatically to the next position. The electron floodgun was active for each irradiation cycle where the pellet was targeted to ensure that no charge could accumulate. The aim of the experiment was to investigate the angular distribution of sputtered particles. To cover the the widest possible angular range, the catcher was moved to several different positions during experiments, usually in 10° increments as illustrated in figure 4. The collection of movements in one angular direction is called a sweep. The beam time was adjusted when using He^+ ions to apply roughly the same fluence on both targets as was the case for the Ar^+ irradiations. For every angular position β of the catcher, the following steps were performed:

1. Turning off the beam and waiting for the drifts to stabilise. Due to the high sensitivity of the quartz frequencies, every movement of either catcher or target results in a signal disturbance which makes rapid measurements impossible. Since the electrons are emitted by the floodgun in a focused beam, the thermal drift also depends on the angular position of the catcher QCM. By default, a waiting period at each position is implemented to allow the system to reach a steady state until the desired irradiation is carried out.

2. First QCM irradiation. The beam is turned on and the QCM is irradiated to gather sputtering data which can be compared to the signal of the pellet.

3. Waiting - drive target holder to pellet position - waiting. At the beginning of this step, the beam is turned off again until irradiation starts.

4. Pellet irradiation. The beam is automatically switched on for irradiation and turned off afterwards.

5. Waiting - drive target holder to QCM position - waiting. The beam is again turned off until the measurement starts.
6. Second QCM irradiation. This second measurement was performed to monitor differences in QCM signals between short time periods and therefore gain insight into potential discrepancies.
7. Waiting - drive catcher to next angular position - waiting. The catcher is automatically rotated to the next angular position and the whole process is repeated.

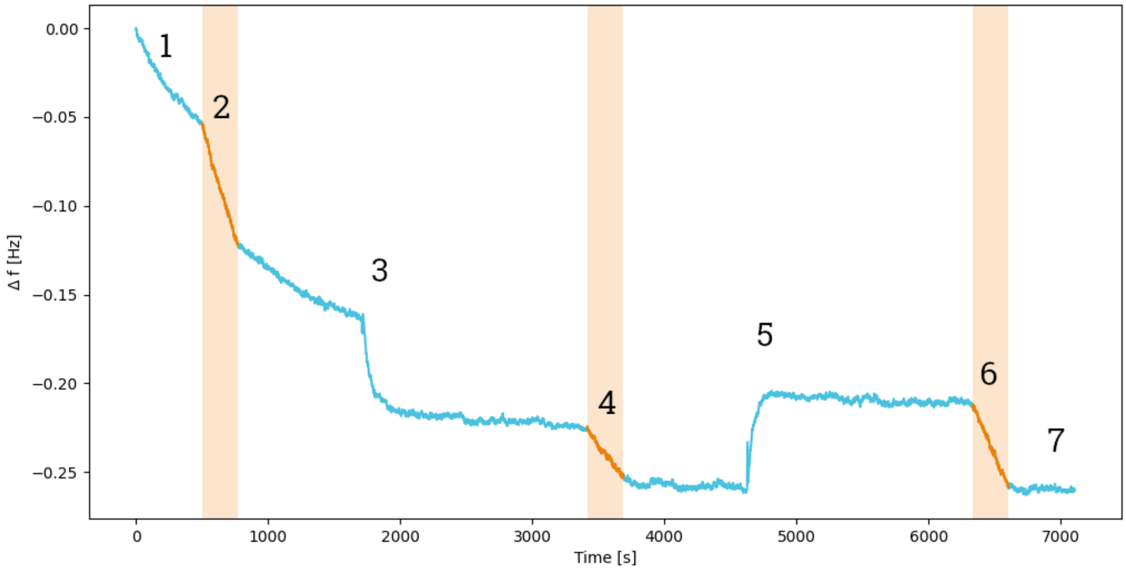

Figure 12: Typical frequency curve for one angular position of the catcher QCM for Ar^+ ions with a kinetic energy of 2 keV under an angle of incidence $\alpha = 60°$. The numbers in the graph indicate the corresponding section of the irradiation process as described in the above list. The parts of the measurements where the ion beam was switched on are indicated by an orange shading.

The two QCM irradiations were included in the experimental workflow to serve as a reference both before and after the irradiation of the pellet, and also to allow signal comparisons between different measurement cycles. The number of sweeps as well as the number of angles within one sweep was adjusted for each measurement depending on the working gas and the total fluence that was considered acceptable for the targets. In general, the beam times for both pellet and QCM were limited to no more than 350 s to minimise the risk of applying too much fluence on the targets since argon measurements were performed as proof-of-principle measurements and also to verify the validity of the PEP-C procedure. For He^+ ions, however, the number of sweeps was increased to gather more data about the sputtering effects. Figure 12 represents a typical frequency curve of the catcher QCM at a fixed angular position. The average slope of one irradiation can be calculated by fitting this curve linearly in the desired time intervals. However, in hindsight, the shortened irradiation lengths in combination with the increased ion fluxes for helium led to frequency curves that were more complicated to interpret properly. Thus, automatically fitting through the whole time span of irradiation was not an appropriate tool for data evaluation anymore. To aide the evaluation process, a new graphical user interface was developed.

5.2 Data Evaluation

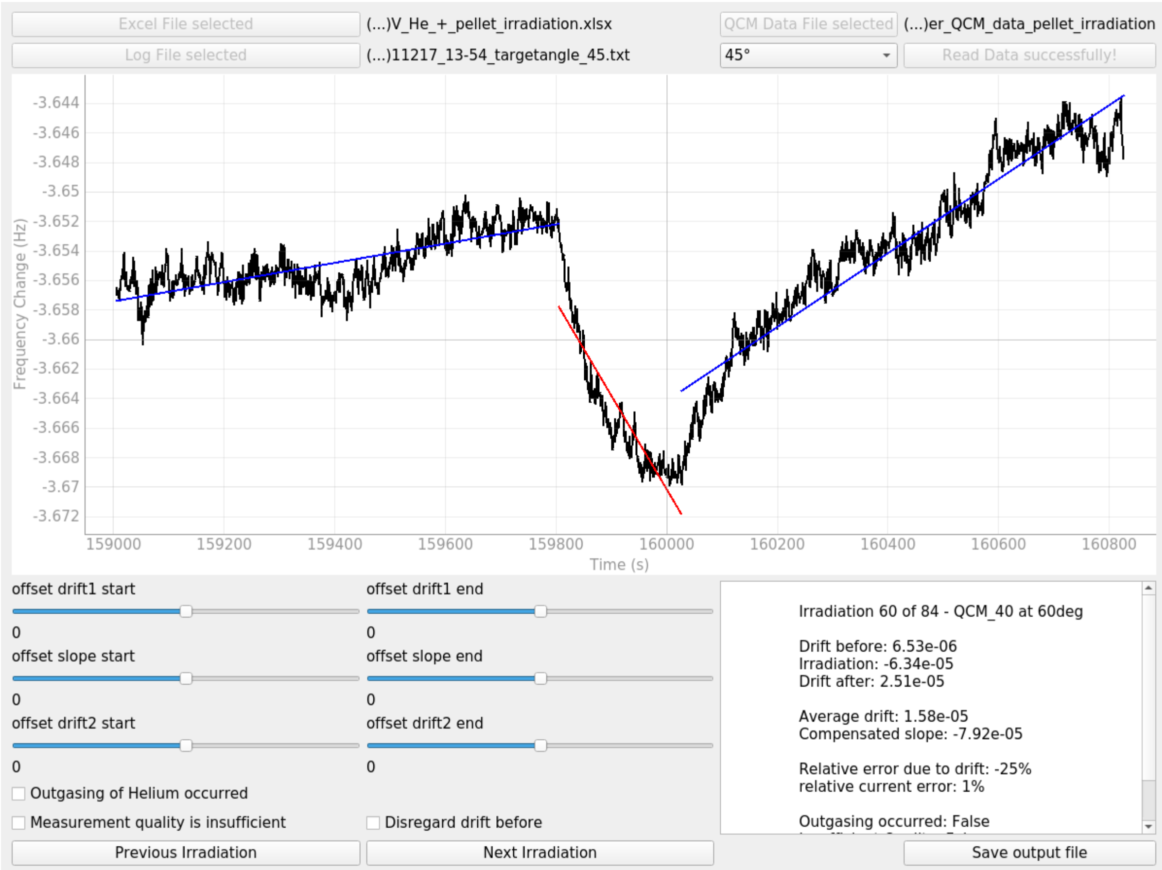

Figure 13: Example of a 4 keV He+ irradiation under $\alpha = 45°$ with respect to the target surface normal. Due to a non-linear irradiation slope the quality of the linear fit is impaired. The accuracy of the fit can be improved by changing the start and end times of the fit. The graphical display is updated immediately, thus enabling the user to assess the quality of the fits more conveniently.

When evaluating measurements it is sometimes the case that the catcher QCM's resonance frequency does not change linearly. However, the standard automated fitting procedure does not take this into account and applies the linear fit regardless. As a consequence, the resulting fits may not be representative of the actual slope before, during or after an irradiation. Figure 12 shows a sample of such a frequency curve. Note that the initially steep irradiation slope flattens off as ion bombardment progresses. The red line represents the linear approximation generated automatically, which differs significantly from the actual curve. In this case, the impact of the shorter irradiation times becomes visible. The program used for evaluation at the time calculated the linear fits only by analysing the frequency values at the beginning and end time stamp of each curve fit. As a consequence, a vast proportion of these fits were determined to be of insufficient quality. Instead of manually adjusting the start and end times of the linear fits by changing sections of the existing code it was decided that this procedure needed to be replaced by a more sophisticated graphical user interface. This newly introduced GUI allows the user to directly change the drift and slope settings for each subsequent irradiation of a catcher sweep while simultaneously portraying and updating the corresponding graphs in real time. The quality of the linear fits for the drifts before and after an irradiation as well as the irradiation slope itself can now be adjusted easily by modifying the start and end times which are immediately passed on to the fit calculation. When applying this evaluation method the accuracy of the linear fits improved to the extent that the resulting data could be used for further evaluation. This proved especially helpful when analysing the measurements conducted with helium ions, which are described in more detail in section 6.2. When exiting the program all the information is stored in a separate output file for each investigated target, which can then be conveniently used to graphically represent the obtained data. It is reasonable to assume that this newly developed analysing tool will render preceding evaluation methods obsolete due to its convenience and the quality of the generated output.

6 Results and Discussion

6.1 Ar^+ on Enstatite ($MgSiO_3$)

Experiments were carried out by using Ar^+ ions with kinetic energies of 2 keV impinging on enstatite targets under an angle of incidence of 45° and 60° with respect to the target surface normal. The catcher position was usually varied in 10° increments between $\beta = -10°$ and $\beta = 60°$ for each sweep. Beam times for pellet and QCM varied between 150 and 350 seconds depending on target condition and ion current for each measurement.

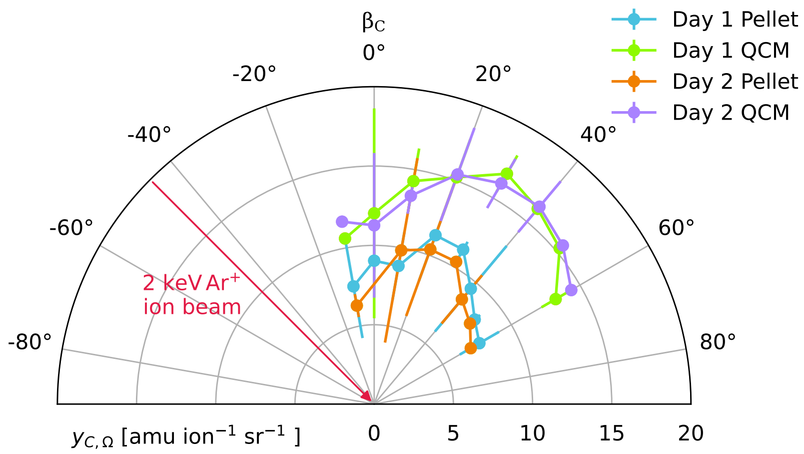

(a)

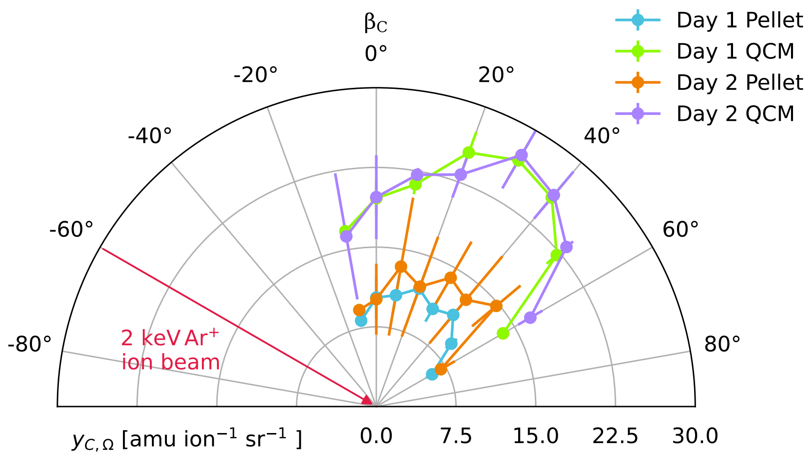

(b)

Figure 14: Results for 2 keV Ar^+ irradiations. (a) shows the catcher signal for QCM and pellet irradiations under $\alpha = 45°$. (b) represents the corresponding measurement under $\alpha = 60°$. Pellet data points are coloured blue for the first measurement series and orange for the second one. The colour of the QCM signals is green and purple, depending on the measurement cycle.

The Ar^+ experiments presented in this thesis were performed as proof-of-principle measurements and consisted of two sweeps with one QCM-Pellet-QCM irradiation at each angular position of the catcher. This measurement process aimed to provide additional reference points for the frequency data obtained from the pellet irradiations and also to quantify the fluence-dependency of the obtained data, if these effects were observed at all. Figure 14 represents the resulting data of these experiments.

Figures 14a and 14b show the measured catcher yields for angles of incidence of 45° and 60°, respectively. The data points of measurements that were conducted under the same impingement angle were plotted on the same diagram to enable easier comparison between them. The r-axis describes the mass deposition on the catcher QCM in amu per incoming ion and solid angle Ω_c at each angular position. When analysing the signals observed on the catcher QCM for both angles of incidence, a clear increase in sputtered target mass can be seen when changing the angle of incidence from 45° to 60°. At a relative catcher angle of around 30°, irradiations of pellet and thin film resulted in the biggest mass removal, which followed expectations [14]. In general, irradiations of the pellet resulted in sputter yields about half as high as the ones observed on the primary QCM. Considering the effects discussed in figure 1, this reduction in sputter yield could be attributed to the pellet's increased surface roughness. To investigate this further and to disentangle roughness effects from other differences between the sample types, simulations have been carried out in a recent manuscript [18, 45]. In these, a ray-tracing approach was applied to account for the geometry of the pellet surfaces. The simulation approach is sketched in [17]. Moreover, the mean of the local inclination angle distribution has been found to be a reliable descriptor for the quantification of roughness effects on the sputter yield [17, 46]. Indeed, surface topography was identified to be the driving factor of this reduction in sputter yield.

It is important to note that each graph of figure 14 shows measurement data of experiments that were performed 14 days apart from one another. When comparing the absolute signals of both pellet and QCM for the different angles the data lie well within the respective error bars. It is therefore concluded that future measurements will be reproducible thanks to the improved preparation process described in section 4 and can be compared quantitatively to one another, thus improving the data evaluation process.

6.2 He^+ on Enstatite ($MgSiO_3$)

To better simulate solar wind flux, a second set of experiments was carried out using He^+ ions with energies of 4 keV impinging on enstatite under an angle of incidence $\alpha = 45°$. Each measurement consisted of several QCM-Pellet-QCM irradiations distributed over relative catcher angles of -10° to 60°. Figure 15 represents the acquired frequency data of the catcher QCM of two measurements that were carried out one week apart from one another.

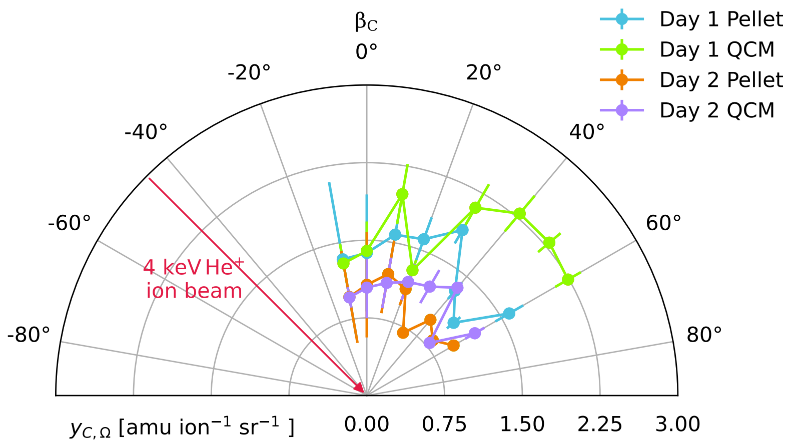

Figure 15: Results of two separate He^+ irradiations with a kinetic energy of 4 keV under an angle of incidence of 45°. The blue data points represent the change in catcher frequency observed when irradiating the pellet whereas the catcher signal for primary QCM irradiations is displayed in orange.

The data points produced during the first irradiation cycle differ significantly from those of the second cycle. Concerning the data points obtained during the first measurement, pellet and QCM irradiations resulted in similar signals. However, no clear relationship between the signals obtained during pellet and QCM measurements is evident in the second cycle. The weak signals for smaller values of beta result in larger uncertainties of the respective slopes, which manifest themselves by bigger error bars in this region of the graph. Also, the distribution of the data points within pellet and QCM irradiations does not conform to the expected pattern, which usually reaches a maximum at a catcher angle of around 40° relative to the target surface normal. Note that the catcher yield of helium is around 10 times lower than the yield observed with Ar^+ ions under the same impact angle. Since the momentum of any particle is described by $p = \sqrt{2Em}$, this can be explained in part by the different kinetic energies and masses of the two projectile types. During the experiments described in this thesis, He^+ ions possessed higher kinetic energies than Ar^+ ions. However, their individual mass is about an order of magnitude smaller. This difference in atomic weight prevailed over the surplus in kinetic energy and resulted in a reduced momentum of the helium particles. As was already described in section 1.2, the momentum of the projectiles influences the resulting sputtering yield.

Figure 15 shows rather peculiar and steep jumps between measurements points. Indeed, a new phenomenon was observed when the operating gas was switched from argon to helium. At certain angular positions of the catcher the QCM's frequency curve showed non-linear behaviour. In most cases, a waiting period of approximately 200 s was sufficient for a stable drift to emerge. Nevertheless, this complicated the data evaluation process since the irradiation times were limited to 350 s to avoid applying too much fluence on the targets. The analysis tool used up until this point in time read in the frequency values at the beginning and end time stamp of each curve section and calculated a linear fit according to the least squares function approximation. However, the curves that the program was analysing did not follow linear behaviour anymore. Hence, when this algorithm was used for the evaluation of helium irradiations, it produced inaccurate linear fits that were only a poor approximation of the actual curve. This complicated the data evaluation process and demanded the introduction of the new graphical user interface which was already described in section 5.2.

Non-linear behaviour was mainly encountered when the catcher was positioned in forward direction with respect to the ion beam. The same phenomenon was already observed and investigated in [8] using a helium ion beam. It might therefore be considered to be caused by the implantation and outgassing of helium ions during and after the respective irradiations or by the stress caused due to the impinging ions. At positions where $\beta \approx \alpha$, the catcher is not only exposed to sputtered target material but also to ions that are reflected by the target. This poses two major problems: On the one hand, the frequency slopes during these irradiations usually start with a steep decline and flatten off as ion bombardment progresses, which makes it difficult to evaluate how big of a change in frequency was induced by sputtered particles. Secondly, a significant increase in resonance frequency is observed directly after the ion beam is switched off. Figure 16 shows a typical frequency curve of the catcher QCM at which a non-linear behaviour was encountered. Note that the slope of the frequency curve flattens off towards the end of the irradiation, where an increase in resonance frequency occurs. After around 200 s the drift after the irradiation stabilises.

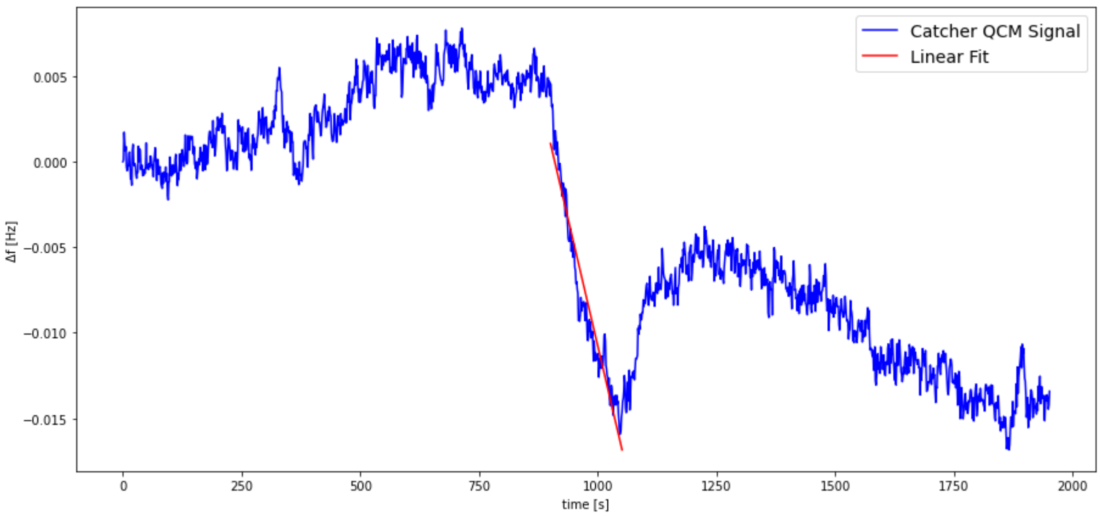

Figure 16: Frequency curve of the catcher QCM during a pellet irradiation under $\alpha = 45°$ with 4 keV He^{+}. The catcher was positioned at $\beta = 20°$. The red line represents the linear fit which is calculated automatically by the evaluation tool. A significant increase in frequency occurs after irradiation has ended which is attributed to the outgassing of implanted ions.

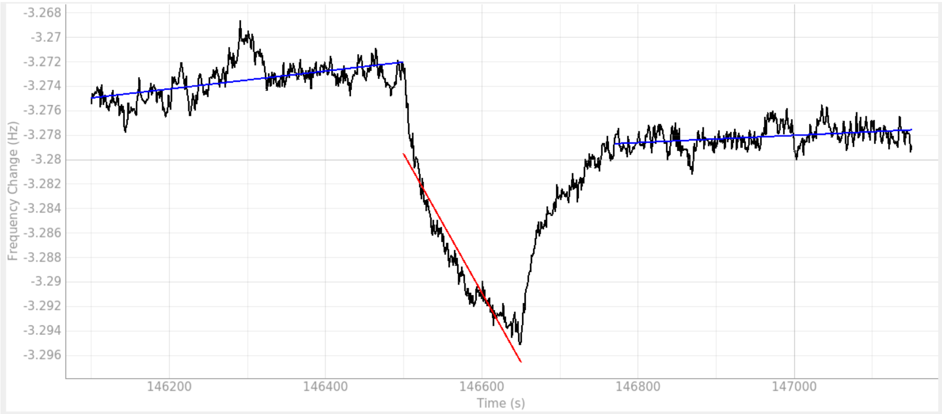

(a)

(b)

Figure 17: Different fitting methods for frequency curves where outgassing is observed. The blue and red lines represents the linear fits for the frequency drifts and the irradiation slope, respectively. (a) shows the regular evaluation process. In (b) the outgassing procedure is used to compensate the irradiation slope by the change in frequency induced by the implantation of helium ions. Note the vast difference in absolute signal between the two methods.

An attempt was made to modify the evaluation GUI in such a way that it automatically compensates the slope depending on the frequency increase directly after the irradiation. This calculation was mainly based on geometrical considerations and aimed to remove the changes in resonance frequency that were caused by implanted ions from the final data. This was done by subtracting the frequency increase during the outgassing of ions from the overall slope. Ideally, in the case where no non-linear slopes occur and the drifts before and after the irradiation are identical, this procedure should have no effect on the output. Figure 18 shows two frequency plots of the same irradiation. In figure 17a the linear fit is calculated by the usual algorithm, whereas the outgassing compensation method is used in figure 17b. Note the clear difference between the two linear fits for the irradiation slope, which are represented by the red lines. To assess the influence of the slope compensation on the final output, the complete helium measurement of the first cycle was evaluated twice. The results of this comparison are shown in figure 18. Note how many of the data points between figures 18a and 18b differ greatly from one another. On the one hand, this is a consequence of the slope compensation, which reduces the frequency slopes in forward direction. On the other hand, the data points for small catcher angles between -10° and 20° seem to increase in signal strength when using the outgassing tool. However, this is also a consequence of individual adjustment of the fits since it is impossible for an individual to completely replicate a whole data evaluation process. This aforementioned sensitivity of the data points to the user input in combination with the inconsistent results generated by the outgassing tool finally lead to the abolishment of this feature. Despite these efforts, no consistent results were achieved using He^+ ions as projectiles in combination with irradiation times in the range of 300 s. In the future, prolonging the timespans of irradiation might lead to the formation of a constant slope of the catcher resonance frequency. This comes at a cost, however: Applying higher fluences leads to subsequent ion beam damages, potentially amorphising the pellet. Therefore, it might not be possible to investigate crystallinity effects simultaneously with the steady state ejecta angular distribution.

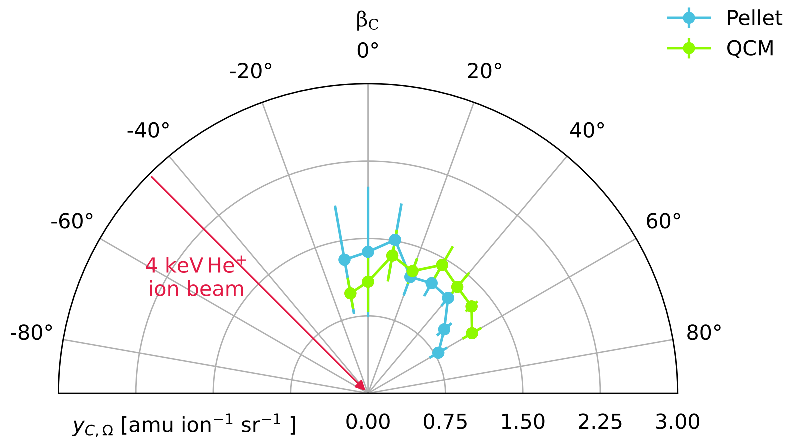

(a)

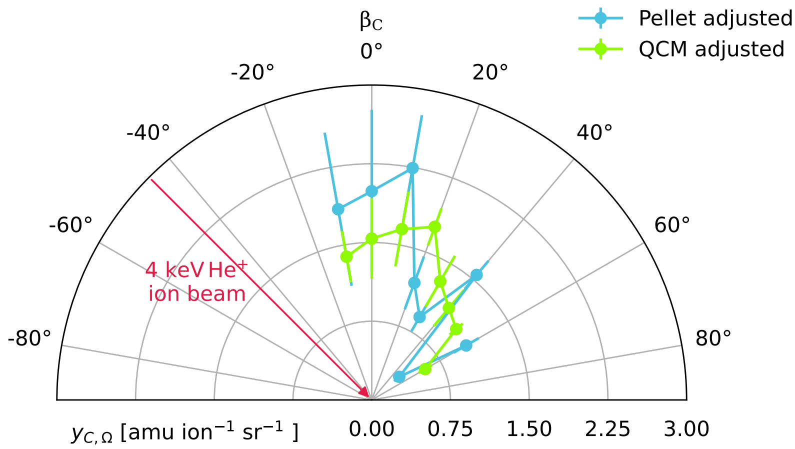

(b)

Figure 18: Difference between data sets resulting from the first helium measurement with 4 keV He^+ ions under $\alpha = 45°$. The data points in (a) were created by analysing the frequency curves without the slope correcting procedure. (b) shows the output of the same measurement where the outgassing procedure was used.

7 Conclusion and Outlook

The catcher QCM setup was used to irradiate a target under $\alpha = 45°$ and $\alpha = 60°$ with respect to its surface normal. Proof-of-principle measurements were performed using 2 keV Ar^+ ions to verify whether the modifications made to the setup including the pre-coating process of the catcher QCM yielded the desired results. These improvements on the apparatus were then used to investigate sputtering behaviour of 4 keV He^+ ions on enstatite in an attempt to gather new data about the effect of solar wind sputtering of mineral samples as realistic proxies for surfaces of rocky bodies in space. During irradiations the sputtered particles were caught by the catcher QCM where mass deposition could be measured by analysing the quartz's eigenfrequency. The distance between target and catcher remained constant throughout all experiments at $r = 17$ mm. Sputtering behaviour was mainly investigated for a pellet made out of ground and pressed $MgSiO_3$ mineral powder to act as a hermean regolith analogue due to its composition, roughness and crystallinity. An enstatite-coated QCM was used to obtain sputter yields and the angular distribution of ejected particles for an amorphous and smooth $MgSiO_3$ target. These data act as a reference and can subsequently be compared to the ones obtained from the pellets.

The primary QCM was irradiated before and after each of the pellet irradiations to provide additional information about possible fluence dependencies of the measurement data. After modifying the setup multiple times and introducing the PEP-C procedure a vast improvement in the consistency of the acquired data was observed. The newly installed Fe-catcher can be sputter cleaned after each irradiation cycle, thus removing the layer that accumulated during experiments. This guarantees the same initial conditions between experiments. By irradiating a pellet area unused during the actual experiments with a focused beam a new homogeneous coating can be applied to its surface before each measurement. This allows for the establishment of a steady state in the catcher QCM's signal before the start of the irradiations.

New effects have to be taken into account when performing irradiation experiments with He^+ ions. One key phenomenon, which occurred frequently at larger catcher angles, was non-linear behaviour of the catcher resonance frequency, possibly due to the implantation of reflected projectile ions into the catcher QCM. It led to anomalies in the frequency signals and complicated the linear fitting of the data. Hence, a new data evaluation GUI was introduced, which allowed manual adjustment of the fitting parameters to improve the quality of the data acquired from the linear regression. However, evaluating frequency curves where outgassing occurred has proven to be a complex task that will require further investigation. During the course of this thesis, it was decided to apply as little fluence as possible on both targets to limit erosion of the film and avoid amorphisation of the pellet. However, longer irradiation times may result in stable frequency changes on the catcher QCM and minimise the uncertainty induced by outgassing effects. Due to the improvements made to the setup and the newly introduced PEP-C procedure it is now possible to perform measurements, which can be compared among one another independent of the time at which they were carried out. This will enable more detailed data analysis between future experiments and will likely provide the basis for upcoming He^+ ion irradiations.

The IAP is scheduled to carry out first irradiation experiments on real lunar regolith samples later in the year. 2.4 g of lunar material were collected during the Apollo 16 mission and are at the moment of writing located at the University of Bern. These upcoming irradiation experiments on real lunar rock will provide information about the validity of the experiments performed on analogue materials and also give further insights into the formation of the moon's exosphere and the sputtering processes involved.

References

[1] Hapke B. Space weathering from Mercury to the asteroid belt. *Journal of Geophysical Research* **106** (2001), pp. 10039–10073.

[2] Pieters C.M. et al. Space weathering on airless bodies: Resolving a mystery with lunar samples. *Meteoritics and Planetary Science* **35** (2000), pp. 1101–1107.

[3] Gold T. The Lunar Surface. *Monthly Notices of the Royal Astronomical Society* **115** (1955), pp. 585–604.

[4] Wurz P. et al. The lunar exosphere: The sputtering contribution. *Icarus* **191** (2007), pp. 486–496.

[5] Vervack R. J. et al. Mercury's Complex Exosphere: Results from MESSENGER's Third Flyby. *Science* **329** (2010), pp. 672–675.

[6] Milillo A., Fujimoto M., Murakami G., et al. Investigating Mercury's Environment with the Two-Spacecraft BepiColombo Mission. *Space Science Reviews* **216** (2020).

[7] Wimmer-Schweingruber R. F. The composition of the solar wind. *Advances in Space Research* **30** (2002), pp. 23–32.

[8] Biber H. et al. Solar wind Helium ion interaction with Mg and Fe rich pyroxene as Mercury surface analogue. *Nuclear Instruments and Methods in Physics Research Section B: Beam Interactions with Materials and Atoms* **480** (2020), pp. 10–15.

[9] Iijima S., Buseck P.R. High resolution electron microscopy of enstatite I: Twinning, polymorphism, and polytypism. *American Mineralogist* **60** (1975), pp. 758–770.

[10] McCoy T. J. et al. The Geochemical and Mineralogical Diversity of Mercury. 2018, pp. 176–190.

[11] Szabo P.S. et al. Solar wind sputtering of wollastonite as a lunar analogue material – Comparisons between experiments and simulations. *Icarus* **314** (2018), pp. 98–105.

[12] Szabo P.S. et al. Dynamic Potential Sputtering of Lunar Analog Material by Solar Wind Ions. *The Astrophysical Journal* **891** (2020), p. 100.

[13] Biber H. Sputtering investigations of wollastonite using solar wind ions. Master's thesis. TU Wien, 2018.

[14] Behrisch R., Eckstein W. Sputtering by Particle Bombardment. Berlin Heidelberg Springer-Verlag, 2007.

[15] Mutzke A. et al. SDTrimSP Version 6.00. *IPP Report* (2019).

[16] Sigmund P. Theory of Sputtering. I. Sputtering Yield of Amorphous and Polycrystalline Targets. *Physical Review* **184** (1969), pp. 383–416.

[17] Cupak C. et al. Sputter yields of rough surfaces: Importance of the mean surface inclination angle from nano- to microscopic rough regimes. *Applied Surface Science* **570** (2021), p. 151204.

[18] Brötzner J. et al. Laboratory measurements to study the sputtering of Hermean surface analogues under He ion impact. *European Planetary Science Congress.* 2022, EPSC2022–849.

[19] Aumayr F., Winter HP. Potential Sputtering. *Philosophical Transactions of the Royal Society of London. Series A: Mathematical, Physical and Engineering Sciences* **362** (2003), pp. 77–102.

[20] Winter HP, Aumayr F. Hollow atoms. *Journal of Physics B: Atomic, Molecular and Optical Physics* **32**.7 (1999), R39.

[21] Shutthanandan V., Zhang J., Ray P.K. Preferential sputtering of heavy isotopes at low incident ion energies. *Surface Science* **392**.1 (1997), pp. L11–L14.

[22] Narayan J. et al. Atomic structure of collision cascades in ion-implanted silicon and channeling effects. *Materials Letters* **3**.3 (1985), pp. 67–72.

[23] Küstner M. et al. The influence of surface roughness on the angular dependence of the sputter yield. *Nuclear Instruments and Methods in Physics Research Section B: Beam Interactions with Materials and Atoms* **145** (1998), pp. 320–331.

[24] Thompson M W. II. The energy spectrum of ejected atoms during the high energy sputtering of gold. *Philosophical Magazine* **18**.152 (1968), pp. 377–414.

[25] Cupak C. Influence of Roughness on Sputter Yields of Tungsten-Coatings relevant for Nuclear Fusion Devices. Master's thesis. TU Wien, 2019.

[26] Hayderer G. et al. A highly sensitive quartz-crystal microbalance for sputtering investigations in slow ion–surface collisions. *Review of Scientific Instruments* **70** (1999), pp. 3696–3700.

[27] Sauerbrey G. Verwendung von Schwingquarzen zur Wägung dünner Schichten zur Mikrowägung. *Zeitschrift für Physik* **155** (1959), pp. 206–222.

[28] Berger B.M. et al. Sputtering measurements using a quartz crystal microbalance as a catcher. *Nuclear Instruments and Methods in Physics Research Section B: Beam Interactions with Materials and Atoms* **406** (2017), pp. 533–537.

[29] Szabo P. Experimental and Simulated Sputtering of Gold, Iron and Wollastonite with a Catcher-QCM Setup. Master's thesis. TU Wien, 2017.

[30] Dobeš K. Erosion of fusion relevant surfaces under ion impact. Doctoral dissertation. 2014.

[31] Eckstein W. Energy distributions of sputtered particles. Nuclear Instruments and Methods in Physics Research Section B: Beam Interactions with Materials and Atoms. *Research Section B: Beam Interactions with Materials and Atoms* **18** (1986), pp. 344–348.

[32] Brötzner J. An Optimised Catcher-QCM Setup to Study the Sputtering of Lunar and Hermean Surface Regolith Analogues. Master's thesis. TU Wien, 2022.

[33] Galutschek E. Development of a 14.5 GHz all-permanent magnet multicharged ECR ion source for remote operation. Doctoral dissertation. TU Wien, 2005.

[34] Galutschek E et al. Compact 14.5 GHz all-permanent magnet ECRIS for experiments with slow multicharged ions. *Journal of Physics: Conference Series*. Vol. 58. IOP Publishing. 2007.

[35] Berger B.M. Laboratory work on plasma-wall-interaction processes relevant for fusion experiments. Doctoral dissertation. 2017.

[36] Voith C. Investigating the Angular Distribution of Sputtered Enstatite Atoms using a Catcher QCM Setup. *Project Report* (2020).

[37] LabVIEW. URL: `https://www.ni.com/de-at/shop/labview.html`. Accessed: 2022-07-13.

[38] Python. URL: `https://www.python.org/`. Accessed: 2022-07-13.

[39] Brötzner J. Development of a Graphical User Interface to remotely control Ion Beam Experiments. *Project Work* (2022).

[40] Brötzner J. A Catcher-QCM Setup for Measuring Sputtering Yields of Wollastonite as Hermean Surface Regolith Analogue. *Project Work* (2020).

[41] Jäggi N. et al. Creation of Lunar and Hermean analogue mineral powder samples for solar wind irradiation experiments and mid-infrared spectra analysis. *Icarus* **365** (2021).

[42] Ramsier R.D., Yates J.T. Electron-stimulated desorption: Principles and applications. *Surface Science Reports* **12**.6 (1991), pp. 246–378.

[43] Stadlmayr R. et al. Fluence dependent changes of surface morphology and sputtering yield of iron: Comparison of experiments with SDTrimSP-2D. *Nuclear Instruments and Methods in Physics Research Section B: Beam Interactions with Materials and Atoms* **430** (2018), pp. 42–46.

[44] Gerdin G., Stygar W., Venneri F. Faraday cup analysis of ion beams produced by a dense plasma focus. *Journal of Applied Physics* **52** (1981), pp. 3269–3275.

[45] Biber H. et al. Sputtering behaviour of rough, polycrystalline Mercury analogs. *Accepted for publication in: Planetary Science Journal* (2022).

[46] Szabo P.S. et al. Analytical model for the sputtering of rough surfaces. *Surfaces and Interfaces* **30** (2022), p. 101924.

List of Figures